MATERIALS PHYSICS AND MECHANICS RESEARCH ARTICLE

Submitted: October 5, 2025 **Revised: November 10, 2025** **Accepted: December 5, 2025**

Configurational force distribution during perovskite phase growth in a ferroelectric film

M. Bakkar [1] ✉, A. Mhemeed Dbes [1], D.V. Avdonyushkin [2], A.S. Semenov [1,2]

[1] Peter the Great St. Petersburg Polytechnic University, St. Petersburg, Russia

[2] Institute for Problems in Mechanical Engineering of the Russian Academy of Sciences, St. Petersburg, Russia

✉ mamadyan1997@gmail.com

ABSTRACT

The propagation of the interphase boundary during the growth of the perovskite phase in a pyrochlore matrix in thin ferroelectric lead zirconate titanate films on a silicon substrate is studied using the methods of configurational force mechanics. A numerical solution of the boundary value problem of the growth of a perovskite inclusion in an initially pyrochlore film is obtained in axisymmetric and three-dimensional formulations. The growth of cylindrical, conical, and spherical inclusions is considered. The growth of single and multiple regularly and irregularly located inclusions were studied. A comparison of the solutions to the problem in linear-elastic and elastoplastic formulations was made. The dependence of the configurational force on the inclusion size and on the distance from the substrate is obtained. In the modeling, the interphase boundary rate was determined by a power-law dependence on the configurational force. Based on the results of finite-element computations of the spatial and temporal distribution of the configurational force and the evolution equation for the growth rate of the interphase boundary, the gradient of the growth axis angle deviation was determined, correlating with the experimental data obtained from X-ray diffraction analysis and scanning electron microscopy.

KEYWORDS

lead zirconate-titanate thin films • spherulitic microstructure • configurational forces • stress relaxation finite-element modeling and simulation

Funding. *This work has been supported by the grant of Russian Science Foundation (grant RSF 25-11-00274).*

Citation: Bakkar M, Mhemeed Dbes A, Avdonyushkin DV, Semenov AS. Configurational force distribution during perovskite phase growth in a ferroelectric film. *Materials Physics and Mechanics*. 2025;53(6): 25–43. http://dx.doi.org/10.18149/MPM.5362025_3

Introduction

Polycrystalline ferroelectric films with a perovskite structure, owing to their high electromechanical properties, have been widely used as FeRAM memory elements [1–5], offering high data storage density and fast operation, as well as in MEMS devices [5–7], microwave electronics [8,9], energy storage devices [1], infrared detectors [1,2], and optical modulators [2]. Thin-film coatings enable device miniaturization and high performance. Modern methods for fabricating thin ferroelectric films are multi-stage technologies based on radio-frequency magnetron deposition of amorphous films at low temperatures and subsequent heat treatment. The pyrochlore → perovskite phase transformation occurs during the final stage of film fabrication, during high-temperature annealing in air at 580 °C.

One of the primary mechanisms for forming the perovskite phase in thin films on silicon substrates is the growth of island structures (Fig. 1(a)) as spherulites [10,11].

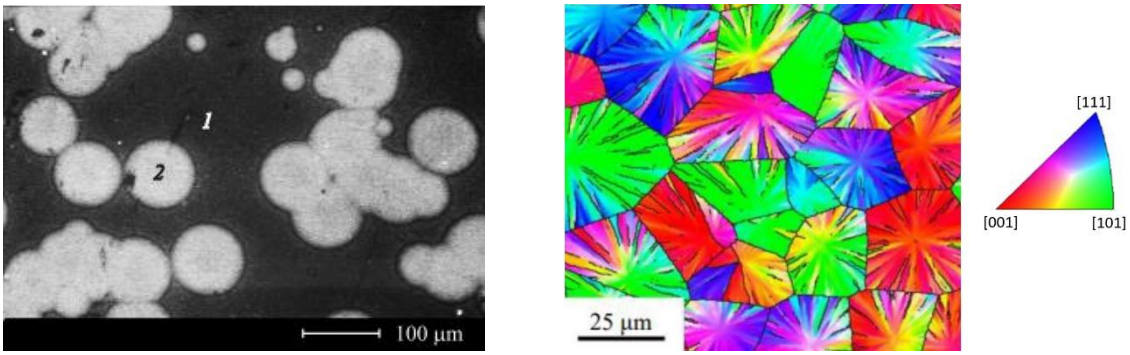

(a) (b)

Fig. 1. Formation of spherulitic structures in thin films of PZT: (a) at the initial stage of growth (data from an optical microscope, 1 – pyrochlore phase, 2 – perovskite phase), (b) at the final stage (maps of crystallographic orientations of growth axes based on the registration of backscattered electron diffraction)

As spherulitic islands merge, a blocky spherulitic microstructure of perovskite with linear boundaries is formed (Fig. 1(b)) [7]. In the case of the studied lead zirconate titanate (PZT) thin films, the phase transition from the pyrochlore phase to the perovskite structure results from a crystallization (recrystallization) process.

During the growth of a spherulite, a progressive deviation of the growth axis from the vertical (normal to the free surface of the film) in the meridional plane is observed. The main cause of this deviation is mechanical stresses arising in the thin film because of a change in volume (-8 %) [12] during the phase transition. The stresses arising during the growth process was evaluated in [12–14]. Due to the deviation of the growth axes, a structure with local axial symmetry is formed within the spherulite, determining the film properties at the macro level.

The relevance of studying residual stresses induced during the film production process and characteristic microstructural parameters of spherulites (size, thickness after shrinkage, angles of deviation of the growth axes, the presence and orientation of defects) is associated with their significant influence on the functional characteristics of ferroelectric films [15–17], dielectric properties [14–17] and hysteresis behavior [15–18].

One of the promising approaches to describing the kinetics of interphase boundaries is the approach of configurational force mechanics (configurational mechanics, mechanics in material space). The origins of configurational force mechanics go back to the work of J.D. Eshelby in 1951 [19], where the concept of a force acting on an elastic singularity (or defect) was introduced. It is defined as the negative gradient of the total energy of a body relative to the position of the defect in the material (not in physical space). The following terms were subsequently used for this force: a configurational force, a driving force, a thermodynamic force (or affinity), a non-Newtonian force, and a material force.

The mechanics of configurational forces have been actively developing since the 1980s as a branch of solid body mechanics, providing a natural description of the evolution of heterogeneities of various natures—from the movement of defects and crack growth to the development of new phase regions and the propagation of chemical reaction fronts. These processes have in common that they cannot be reduced to the displacement of material points under the action of mechanical forces but lead to a change in the configuration of the body due to the movement of defects and boundaries

relative to the material points, i.e., in the material space. Various theoretical and applied aspects of configurational mechanics can be found in [20–31].

The aim of this study is to investigate the kinetics of the pyrochlore → perovskite interphase boundary during high-temperature annealing by analyzing the spatial distribution of configurational forces during perovskite inclusion growth. The growth of inclusions with various initial configurations, including cylindrical, conical, and spherical, is considered. A solution to the problem is obtained in both linear-elastic and elastic-plastic formulations. The latter formulation allows for indirect consideration of dislocations, micropores, and microcracks. To evaluate the mutual influence of inclusions during growth, a solution to the problem for multiple irregular inclusions in a three-dimensional formulation is considered. The results are verified by comparing the calculated gradient of the growth axis deviation angle with experimental data.

Materials and Methods

The objects of the study were thin polycrystalline films of $Pb(Zr_{1-x}Ti_x)O_3$ (PZT) [15]. The composition of the binary solid solution $(1-x)PbZrO_3-xPbTiO_3$ corresponded to the morphotropic phase boundary (MPB), where tetragonal and rhombohedral phases coexist at a ratio of x(Ti/Zr) ≈ 46/54, leading to optimal piezoelectric properties.

The PZT thin films were fabricated in a two-step process using radio-frequency magnetron sputtering of a ceramic target. The substrate used was a <100> - oriented silicon wafer with sequentially deposited layers of silicon dioxide (SiO_2, ~ 300 nm thick) and platinum (Pt, 80 nm thick) [12]. The resulting film thickness was 500 nm, deposited at a temperature of 160 °C. As-deposited films were initially amorphous. Subsequent annealing (1 h) in an air atmosphere at temperatures above 450 °C resulted in the formation of a pyrochlore structure. The phase transformation from pyrochlore to perovskite began at 530 °C, initiating the formation of islands (perovskite inclusions). To obtain continuous perovskite films, the annealing temperature was increased to 580 °C [10].

The average size of the resulting spherulitic blocks ranged from 10 to 40 μm. This grain size was controlled by varying the target-to-substrate distance from 30 to 70 mm during deposition, which correspondingly varied the substrate temperature from 90 to 160 °C. The growth axis deviation angle was characterized using scanning electron microscopy (Lira 3 Tescan, EVO-40 Zeiss) in both backscattered electron and electron backscatter diffraction modes, as well as by θ-2θ X-ray diffraction (XRD) (Rigaku Ultima IV) [13]. The stress-strain state computations were performed using the finite element program ANSYS 2022 R2.

Model of perovskite phase growth in a thin film

The boundary-value problem describing the growth of a perovskite inclusion within an initially pyrochlore film on a silicon substrate was solved in axisymmetric and three-dimensional formulations, as shown in Fig. 2. The axisymmetric formulation is less computationally demanding and enables multivariate calculations with varying inclusion geometries, whereas the three-dimensional formulation provides a more accurate representation of the interactions between neighboring inclusions. In the computations, the inclusion shape (cylindrical, conical, or spherical) and its characteristic dimensions

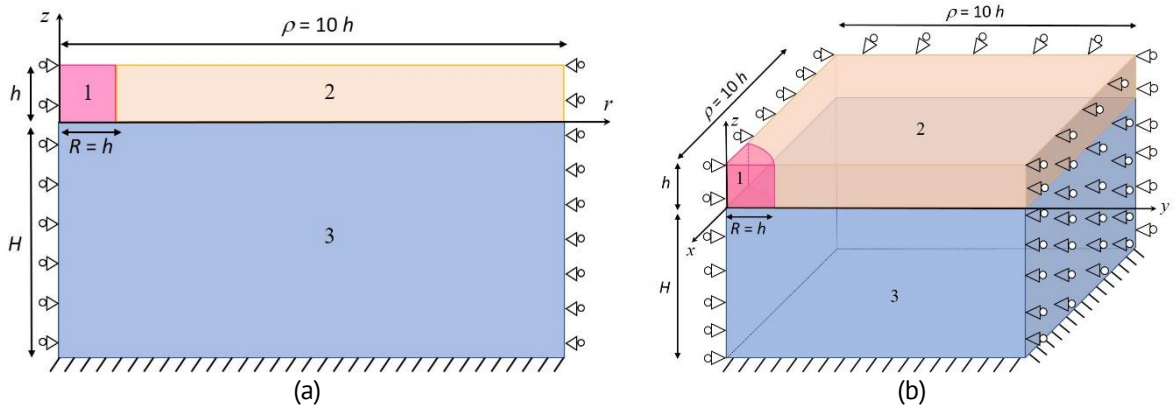

Fig. 2. Geometry parameters and boundary conditions for representative volume element of PZT film in (a) axisymmetric model, (b) 3D model. The material system consists of the perovskite inclusion 1, the pyrochlore matrix 2 and the silicon substrate 3

were varied, (R is the inclusion radius, 2ρ is the distance between inclusion centers, γ is the cone angle).

During the phase transition from pyrochlore to perovskite, there is an 8 % reduction in volume [12], which is the main source of stress in the film. The stresses are determined by the transformation strain tensor:

$$\boldsymbol{\varepsilon}^{tr} = \varepsilon^{*}\mathbf{1} = \frac{1}{3}\frac{\Delta V}{V}\mathbf{1}, \quad (1)$$

where $\mathbf{1}$ is the unit tensor, ΔV is the volume reduction under the phase transition, ε^{*}= 8/3 %. Note that the transformation strain tensor has nonzero value only in the inclusions. It is zero in the pyrochlore matrix and substrate. The constitutive equation of thermo-elasto-chemo-plasticity within the framework of infinitesimal mechanics is defined by the expression:

$$\boldsymbol{\sigma} = {}^{4}\boldsymbol{C}\colon(\boldsymbol{\varepsilon} - \boldsymbol{\varepsilon}^{tr} - \boldsymbol{\varepsilon}^{p} - \boldsymbol{\varepsilon}^{T}), \quad (2)$$

where $\boldsymbol{\sigma}$ is the stress tensor, ${}^{4}\boldsymbol{C}$ is the fourth-order elastic moduli tensor, $\boldsymbol{\varepsilon} = (\nabla\boldsymbol{u})^{S}$is the total strain tensor, $\boldsymbol{\varepsilon}^{p}$ is the plastic strain tensor defined at the active loading by relation:

$$\dot{\boldsymbol{\varepsilon}}^{p} = \frac{1}{H'}\frac{\partial F}{\partial \boldsymbol{\sigma}} \otimes \frac{\partial F}{\partial \boldsymbol{\sigma}}\colon\dot{\boldsymbol{\sigma}}, \quad (3)$$

with $F = \sqrt{3/2\mathrm{dev}(\boldsymbol{\sigma})\colon\mathrm{dev}(\boldsymbol{\sigma})} - H(\varepsilon^{p})$ is von Mises yield function, $\mathrm{dev}(\boldsymbol{\sigma}) = \boldsymbol{\sigma} - \frac{1}{3}\mathrm{tr}(\boldsymbol{\sigma})\mathbf{1}$ is the stress deviator, $H' = dH/d\varepsilon^{p}$ is the slope of the stress-strain curve (isotropic hardening is assumed), $\boldsymbol{\varepsilon}^{T}$ is the temperature strain tensor:

$$\boldsymbol{\varepsilon}^{T} = \alpha\Delta T\mathbf{1}, \quad (4)$$

here α is linear thermal expansion coefficient.

The appearance of mechanical stress slows down the advance of the interphase boundary. In the configurational force method, the rate of advance of the interphase boundary along the normal can be written as [14]:

$$V_N = A|f_N|^{n-1}f_N, \quad (5)$$

where V_N is the interface propagation velocity in interface normal direction, f_N is the configurational force:

$$f_N = \boldsymbol{N}\cdot[[-\boldsymbol{b}]]\cdot\boldsymbol{N}, \quad (6)$$

where $\boldsymbol{N}$ is the normal vector to the interface boundary, $\boldsymbol{b}$ is Eshelby energy-momentum tensor:

$$\boldsymbol{b} = \psi\mathbf{1} - \boldsymbol{\sigma}\cdot\boldsymbol{\varepsilon}, \quad (7)$$

where ψ is the volume density of free energy defined by expression:

$$\psi = \frac{1}{2}(\boldsymbol{\varepsilon} - \boldsymbol{\varepsilon}^{tr} - \boldsymbol{\varepsilon}^{p} - \boldsymbol{\varepsilon}^{T}) : {}^{4}\boldsymbol{C} : (\boldsymbol{\varepsilon} - \boldsymbol{\varepsilon}^{tr} - \boldsymbol{\varepsilon}^{p} - \boldsymbol{\varepsilon}^{T}) + \psi_0(T), \quad (8)$$

here $\psi_0(T)$ is the chemical free energy density, which depends on temperature. It is assumed that the jumps $[\![\varepsilon^*]\!] \neq 0$ and $[\![\psi_0]\!] \neq 0$ in the phase transformation.

The non-uniform configurational force distribution along the film thickness leads to different interface propagation velocities depending on the vertical coordinate *z*. This leads to the tilting of the initially vertical boundary (for linear dependencies $V_N(z)$) and the curvature of the initially straight boundary (for nonlinear dependencies $V_N(z)$). The orientation of the interphase boundary determines the orientation of the growth axis of the formed perovskite.

The main feature of the spherulite ferroelectric structure is the near to linear dependence of the rotation angle β of the growth axis on the coordinate along the radius of the spherulite. Assuming that the rotation is caused by the action of configurational forces, we can obtain an expression for the gradient of the growth axis angle [14]:

$$\frac{\partial \beta}{\partial r} = cos^{\,2}(\beta)\frac{n}{f}\frac{\partial f}{\partial z}. \quad (9)$$

The dependences $\beta(r, z = h)$ for various spherulites were measured experimentally [10] based on X-ray diffraction analysis and scanning electron microscopy methods. With linear changing β from r the value of $\frac{\partial \beta}{\partial r}$ is constant and can be used for validation of the model.

Results and Discussion

The purpose of the computations was to determine the stress distribution, and the associated configurational forces near the interphase boundary. Three types of inclusions were considered: cylindrical, conical, and spherical. The multi-variant finite element computations were performed for regular and non-regular inclusion systems with different sizes of perovskite inclusions. The material parameters [12] used in the solution process are given in Table 1.

Table 1. The material parameters used in the computations

	E, MPa	*v*	α, 1/°C	σ_{02}, MPa
Perovskite	70 000	0.3	$9.0 \cdot 10^{-6}$	500
Pyrochlore	70 000	0.3	$9.3 \cdot 10^{-6}$	-
Silicon substrate	109 000	0.3	$4.2 \cdot 10^{-6}$	-

The rate of radial change in the deviation angle of the growth axis is determined for the jump value $[\![\psi_0]\!]$ equal to 650 MJ/m^3. The data on the change in enthalpy from [32] for $La_2Ti_2O_7$ served as a guideline for setting this value.

Axisymmetric model

Cylindrical inclusion. The cylindrical representative volume element with the radius equal to half the distance between the centers of inclusions ($\rho = 10h = 5$ μm) is used for an axisymmetric formulation of the problem. To describe the evolution of the perovskite inclusion growth process, its radius *R* varied in the range from *h* to 10*h* with a step of *h*. The film thickness *h* was 0.5 μm, and the substrate thickness *H* in the model was 5 μm.

The significant excess of the actual substrate thickness relative to the model was taken into account by the fixed boundary condition on the bottom surface.

The boundary value problem was solved using the ANSYS APDL software package. The finite element mesh (Fig. 3) included maximum 200 elements through the film thickness and a total of 160 000 elements. A quadratic quadrilateral element formulation was used.

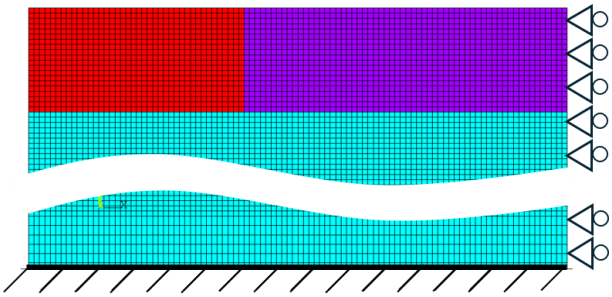

Fig. 3. Axisymmetric finite-element model of a *cylindrical* inclusion growth on a substrate

Configurational force was calculated using a component-wise stress formulation expressed in cylindrical coordinates:

$$f_N = \sigma_{rr}\varepsilon^* - \frac{1}{2E}\left[\!\left[\sigma_{\varphi\varphi}^2 + \sigma_{zz}^2 - 2\nu\sigma_{\varphi\varphi}\sigma_{zz}\right]\!\right] + f_0, \quad (10)$$

where $f_0 = [\![\psi_0]\!]$. To easily compare different formulations, only the stress-dependent part of configurational force is considered below, without f_0.

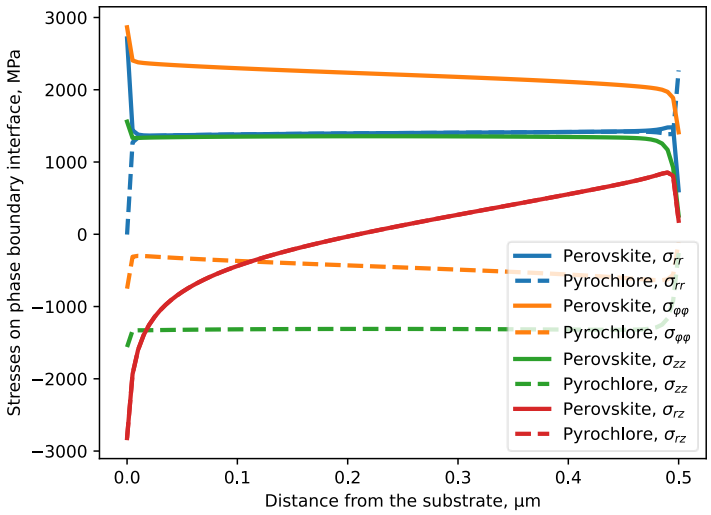

Fig. 4. Dependences of stress tensor components σ_{rr}, σ_{zz}, $\sigma_{\varphi\varphi}$, σ_{rz} [MPa] on the distance from the substrate (vertical coordinate z) for the inclusion radius R equal $5h$ in the model of cylindrical growth of perovskite phase. Distance between inclusion centers $2\rho = 20h$

This boundary value problem was solved in elastic and elastoplastic formulations. *Elastic solution*. The dependences of stress tensor components σ_{rr}, σ_{zz}, $\sigma_{\varphi\varphi}$ and σ_{rz} on the distance from the substrate (vertical coordinate z) for the inclusion radius R equal $5h$ are presented in Fig. 4. The distributions of stress components have a close to linear character over a significant part of the film thickness. Local deviations are observed only on the free surface and near the substrate.

The stress components σ_{rr} and σ_{rz} are continuous at the vertical interphase boundary. The stress components σ_{zz} and $\sigma_{\varphi\varphi}$ undergo a discontinuity (a jump) at the interphase boundary. Figure 4 shows the stress values both to the left of the boundary (in perovskite) and to the right of the boundary (in pyrochlore). Because of the high stress values at the interphase boundary, the circumferential $\sigma_{\varphi\varphi}$ and radial stress σ_{rr} components are the most critical. They are likely to be the main cause of the radial and ring cracks observed in the spherulitic structure.

The evolution of radial stress σ_{rr} and the configurational force f_N distributions with increasing inclusion radius R is shown in Fig. 5. With an increase in the radius of the inclusion R, the radial stress σ_{rr} change from a decreasing dependence on the distance from the substrate z for $R/h = 1$ to a monotonically increasing dependence for $R/h \geqslant 2$ (see Fig. 5(a)). Conversely, the configurational force increases steadily from 0 to $R/h \geqslant 8$, then starts decreasing at $R/h = 9$ as z grows (see Fig. 5(b)).

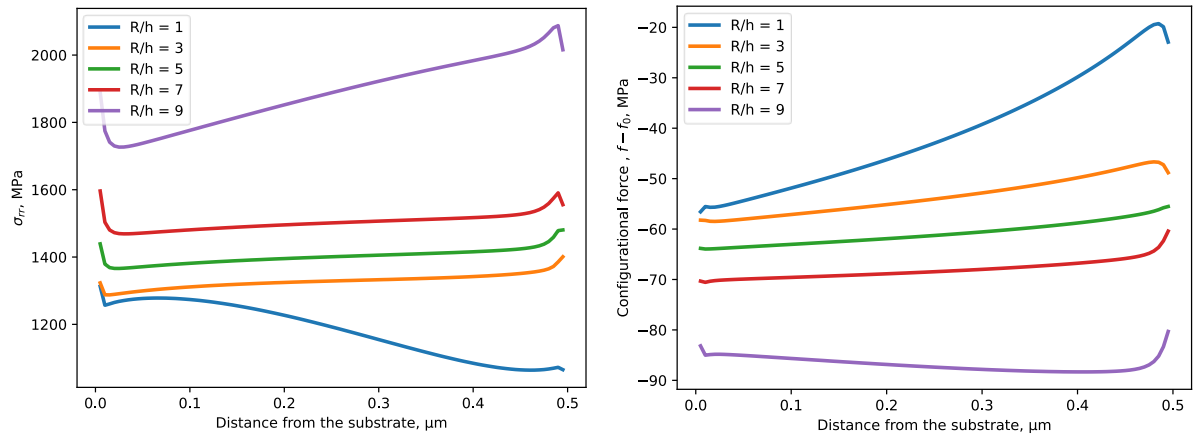

(a) (b)

Fig. 5. Dependences of (a) the radial stress component σ_{rr} [MPa] and (b) the configurational force f_N on the distance from the substrate (vertical coordinate z) for various ratios of the nucleation radius to the film thickness *R/h,* in a model of cylindrical growth of perovskite phase. Distance between inclusions $2\rho = 20h$

For cylindrical inclusions, the monotonically increasing configurational force $f_N(z)$ (Fig. 5(b)) leads in according with Eq. (5) to a progressive deviation of both the interphase boundary and the growth axis from the vertical with the increasing inclusion radius R. The initially cylindrical inclusion will gradually transform with increasing R, into a truncated conical inclusion with a larger radius on the free surface and a smaller radius on the substrate. It should also be noted that there is a surface layer in which the behavior of the angle differs slightly from that of the main part of the film. Growth angle deviation rate according to Eq. (9), with $n = 0.32$ and $z = h/2$ equals 1.1 deg/μm, which corresponds to the order of magnitude observed in experiments ~0.5÷1.4 deg/μm [10–14].

Elastoplastic solution. The elastoplastic formulation allows us to take into account qualitatively the elastic stress relaxation and the appearance of dislocations, micropores, and microcracks observed in experiments. To account for plastic deformation in perovskites, a basic isotropic hardening model based on the plastic flow theory is applied. The hardening modulus was taken to be one hundredth of the Young's modulus.

The resulting stresses and configurational forces for the case of an inclusion radius equal to 5h in the elastic–plastic formulation are presented in Fig. 6(a) and Fig. 6(b), respectively. The dependency of the configurational force $f_N(z)$ is significantly modified by plastic deformation in perovskite. Due to plastic deformations, the stress in perovskite decreases, which leads to a significant increase in configurational forces.

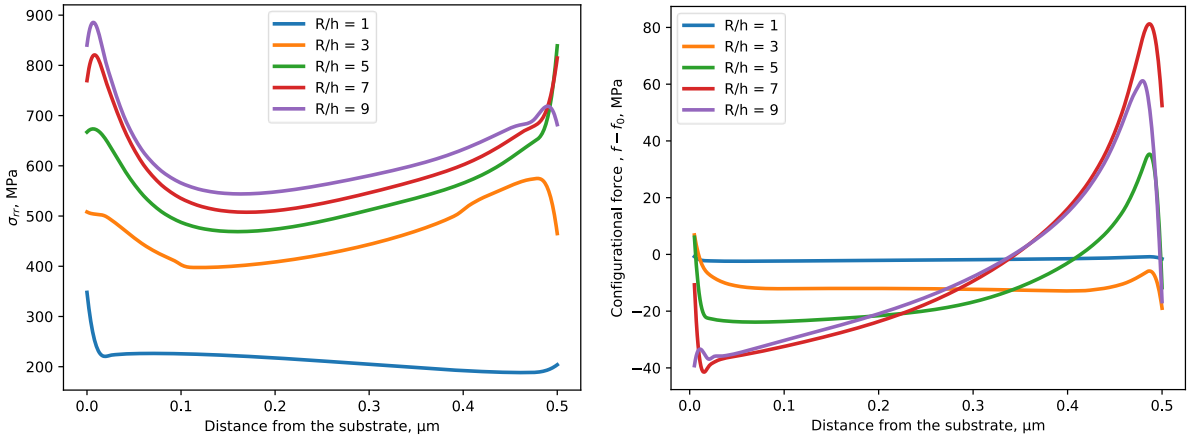

(a) (b)

Fig. 6. Dependence of (a) the radial stress component σ_{rr} [MPa] and (b) the configurational force f_N on the distance from the substrate (vertical coordinate z) for various ratios of the nucleation radius to the film thickness R/h in the model of cylindrical growth of perovskite phase. Distance between inclusion centers $2\rho = 20h$

Unlike the elastic solution, the monotonicity of the configurational force across the film thickness does not depend on the radial coordinate. This feature ensures a monotonic increase in the angle of rotation of the growth anisotropy (Fig. 7). Growth angle rotation rate according to Eq. (9), with $n = 0.07$ and $z = h/2$ equals 0.8 deg/μm, which corresponds to the order of magnitude observed in experiments ~0.5 ÷ 1.4 deg/μm.

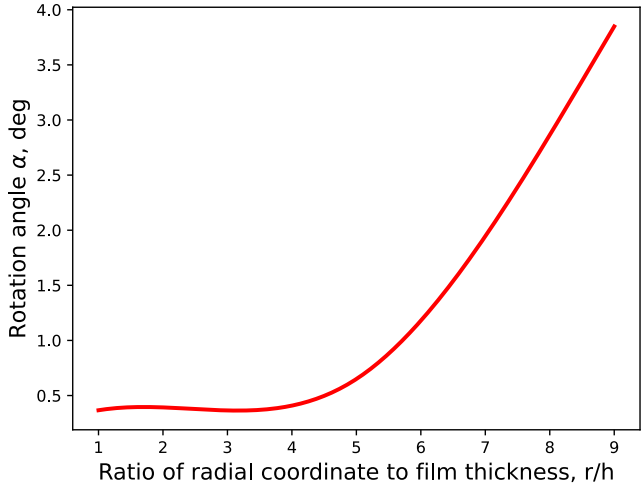

Fig. 7. Rotation angles along spherulite radius

Within the elastoplastic formulation, a distinct linear segment in the evolution of the anisotropy rotation angle is observed. In contrast, the purely elastic formulation reproduces only the order of magnitude of the effect, while failing to capture its qualitative behavior observed experimentally [14].

Conic inclusion. To simulate the growth process, a series of calculations was performed in which the cone solution angle varied from −30° to 30° in steps of 10°, and the radius of the lower base of the cone ranged from 1 to 9 units in steps of 2. A similar set of boundary conditions was analyzed for a cylindrical inclusion.

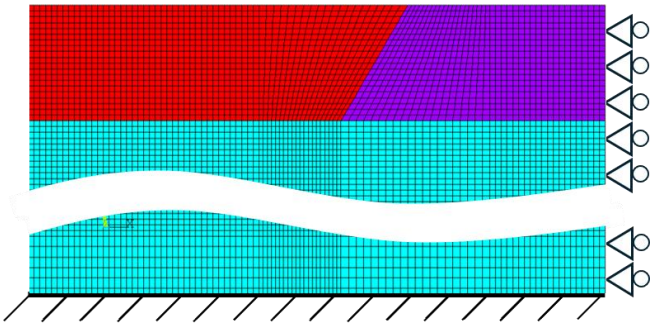

Fig. 8. Axisymmetric finite-element model of a *conic* inclusion growth on a substrate

The expression below is used to calculate the configurational forces for a conical inclusion, similar to Eq. (10):

$$f_N = \sigma_{NN}\varepsilon^* - \frac{1}{2E}\left[\!\left[\sigma_{\varphi\varphi}^2 + \sigma_{LL}^2 - 2\nu\sigma_{\varphi\varphi}\sigma_{LL}\right]\!\right] + f_0, \qquad (11)$$

where $f_0 = [\![\psi_0]\!]$, σ_{NN} is the normal stress to the conical interphase surface, σ_{LL} is the stress component along the cone generatrix.

The dependence of the configurational force on the radial coordinate in the case of a conical model does not differ qualitatively from the cylindrical inclusion model (see Fig. 9(b)). However, the size of the boundary region in which the behavior deviates significantly from linearity increases compared with the case of a cylindrical inclusion.

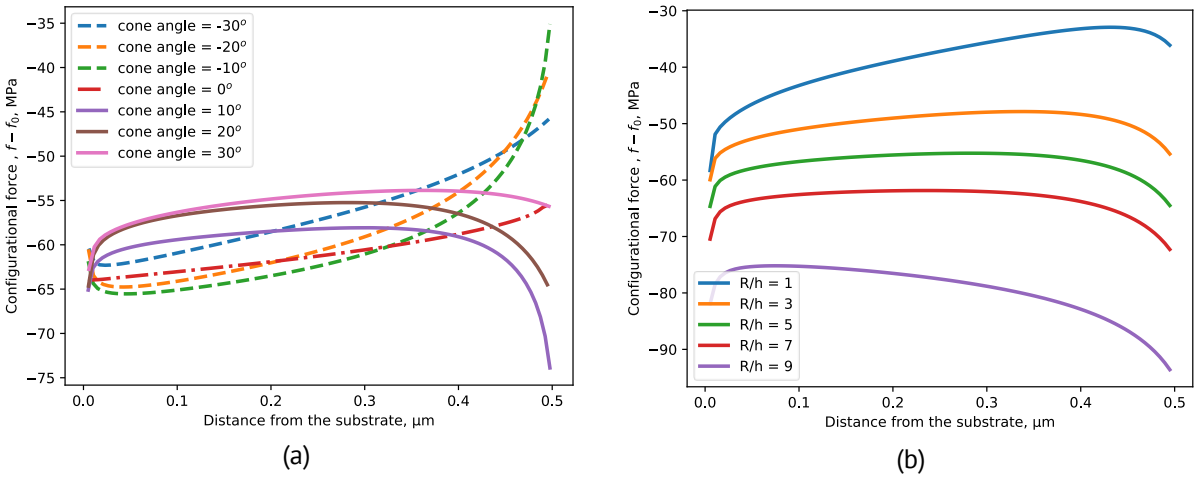

Fig. 9. Comparison of the configurational forces f_N at different (a) cone angles (R/h = 5) and (b) ratios of inclusion radius to the film thickness R/h (cone angle 20°) in the model of conic growth of perovskite phase. Distance between inclusion centers $2\rho = 20h$

When the cone solution angle varies, the monotonicity of the configurational force distribution also changes. For positive angles, the interphase boundary velocity calculated using Eq. (5) is higher near the lower base of the cone. For negative angles, the maximum values are observed near the upper base. The dependence of the configurational force on the angle of the cone shows that the configurational forces tend to bring the inclusion to a near to cylindrical state (Fig. 9(a)).

Spherical inclusion. Two locations of the spherical inclusion were considered: on the free surface of the film and on the substrate (Fig. 10). The radii of spherical inclusions were considered equal to $h/3$. Boundary conditions similar to those in the cylindrical inclusion problem were used.

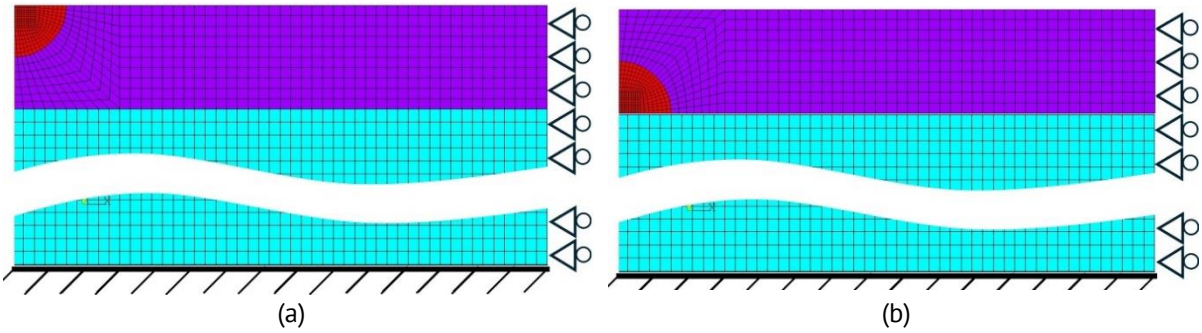

Fig. 10. Axisymmetric finite-element model of the growth of a spherical inclusion with a center on (a) the film free surface, (b) the substrate

From the dependence of the configuration force (Fig. 11), it can be seen that in a spherical inclusion on a substrate, growth in the direction of the film thickness prevails, while on the film surface, the inclusion grows in the radial direction. At large radius, the curvature of interphase boundary decreased, and the model of a spherical inclusion reduces to a conical inclusion.

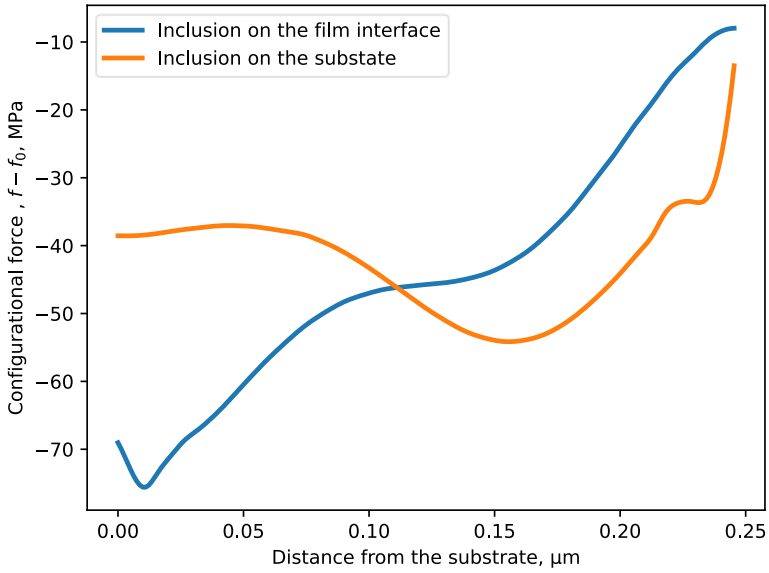

Fig. 11. Configurational forces for a spherical inclusion. The distance is measured from the lowest point of inclusion. Inclusion radius is equal to $h/3$

Three-dimensional model

Single cylindrical inclusion. A three-dimensional model was used to assess the interaction of nearby cylindrical perovskite inclusions on stress fields and configurational forces. The three-dimensional model has the same geometry and boundary conditions with the prior axisymmetric case (see Section "Axisymmetric model"). The *first model* corresponds to a single symmetrical perovskite inclusion (see Fig. 12) with a cylinder radius R varied from 0.5 to 4.5 μm, a film thickness h of 0.5 μm, and a substrate thickness of 5 μm. The radius of the cylinder was then increased incrementally in order to simulate the development of the perovskite phase. This case corresponds to the regular (periodic) inclusion system.

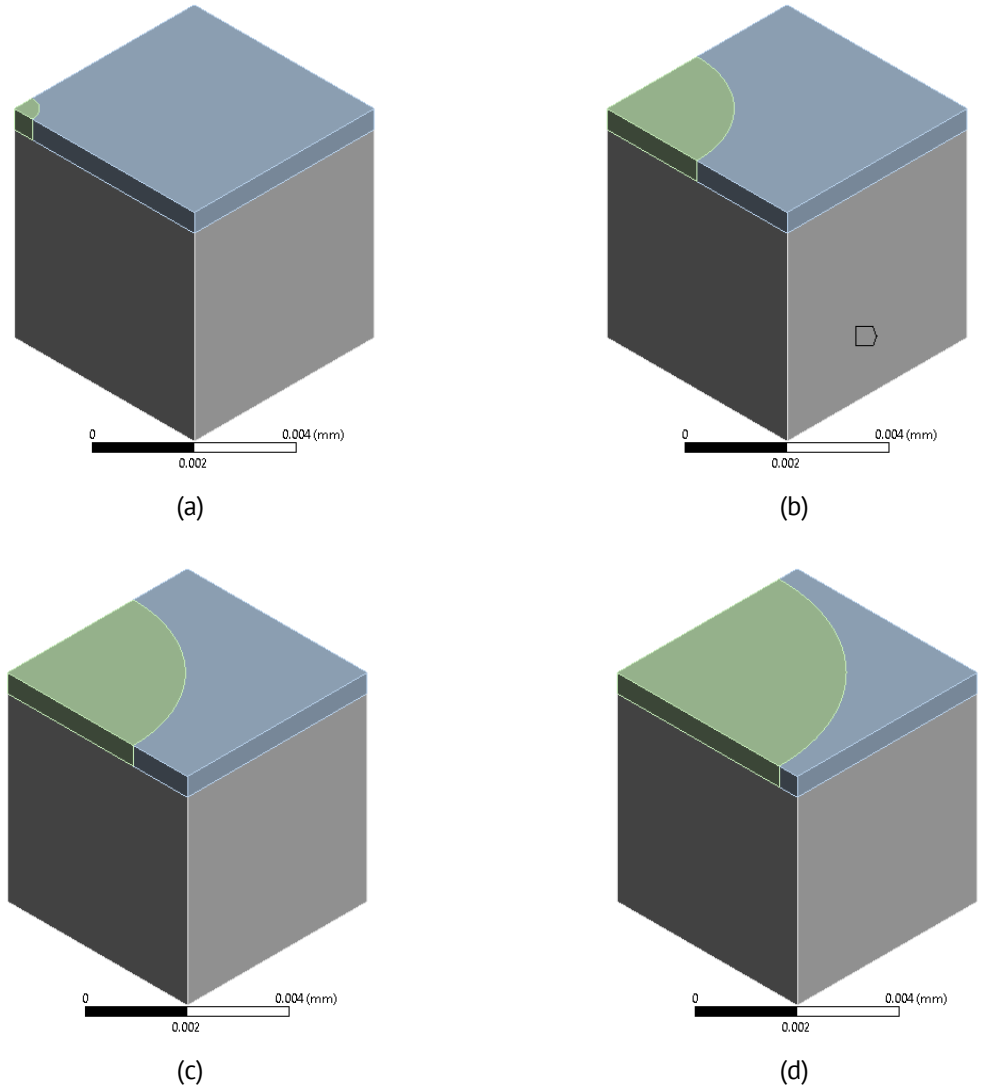

Fig. 12. 3D models of the cylindrical perovskite inclusion growth on a substrate: (a) $R/h = 1$, (b) $R/h = 5$, (c) $R/h = 7$, (d) $R/h = 9$. Distance between inclusion centers $2\rho = 20h$

The *second model* corresponds to the non-regular inclusion system with a more realistic scenario for the growth of perovskite inclusions in a pyrochlore matrix (Fig. 1(a)). The study focused on six adjacent perovskite inclusions. A key feature of the experiment was that the centers of these inclusions were positioned at varying distances from one

another. The considered model with an irregular (non-periodic) arrangement of inclusions allows for a more detailed study of the effects of interaction between inclusions, paying particular attention to such parameters as stress and configuration force.

Under identical boundary conditions, the differences in the radial, circumferential, and vertical stress values for the three-dimensional and two-dimensional axisymmetric models were 2, 9.7, and 2.7 %, respectively (compare Figs. 4 and 13) in elastic solutions, for an inclusion radius R/h = 5. Similar to the two-dimensional model, the maximum stress jump between the perovskite and pyrochlore phases was found to be the jump in vertical and circumferential stress.

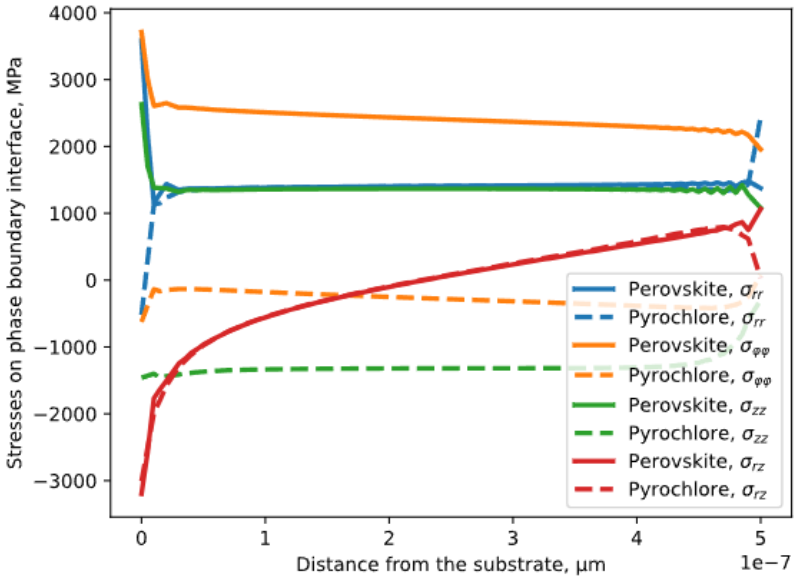

Fig. 13. Dependences of the stress tensor components σ_{rr}, σ_{zz}, $\sigma_{\varphi\varphi}$, σ_{rz} [MPa]on the distance from the substrate (vertical coordinate z) for the inclusion size R/h = 5h in the 3D model of cylindrical growth of the perovskite phase. The distance between inclusion centers is 2ρ = 20h

A comparison of the configurational forces in the three-dimensional and two-dimensional axisymmetric models revealed differences in the results only for inclusion radii R exceeding 0.90 of the half-distance between inclusions ρ. At smaller radii, the inclusions do not interact with each other. The results indicate that the maximum discrepancy in configuration forces between the two models in this case is 8 % (Fig. 14). This result demonstrates the potential of using a highly accurate two-dimensional symmetric model to reduce the computational costs associated with calculating configuration forces.

In order to comparison between three-dimensional models and a two-dimensional symmetric model with respect to configuration force, it was necessary to choose an inclusion radius that was nine times greater than the film height. This approach enabled the selection of the influence of inclusions on each other. In the case of small radii, inclusions do not affect each other. The findings indicate that the maximum disparity in configuration forces between the two models is 8 % in the studied case (Fig. 14). This result indicates the possibility of using a two-dimensional axisymmetric model to reduce the computational costs associated with calculating configuration forces.

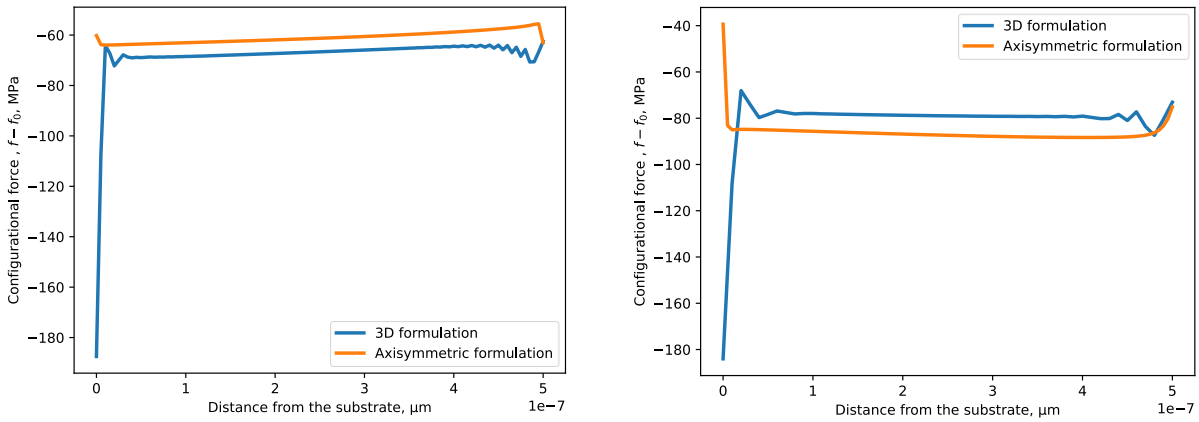

Fig. 14. Comparison of the two-dimensional symmetric with the 3D solution for the configuration force f_N for R/h=5 and R/h=9. The distance between inclusion centers is 2ρ = 20h

Multiple cylindrical inclusions. A three-dimensional simulation is considered using a representative configuration of six inclusions, the spatial arrangement of which was obtained from available literature (see Fig. 1). Within the three-dimensional model, the influence of inclusion distribution on both the stress-strain state and the configurational force was investigated. Changes in the distances between inclusions at successive growth stages were examined according to the attainment of radii of 2.5, 5, 7.5, and 10 μm.

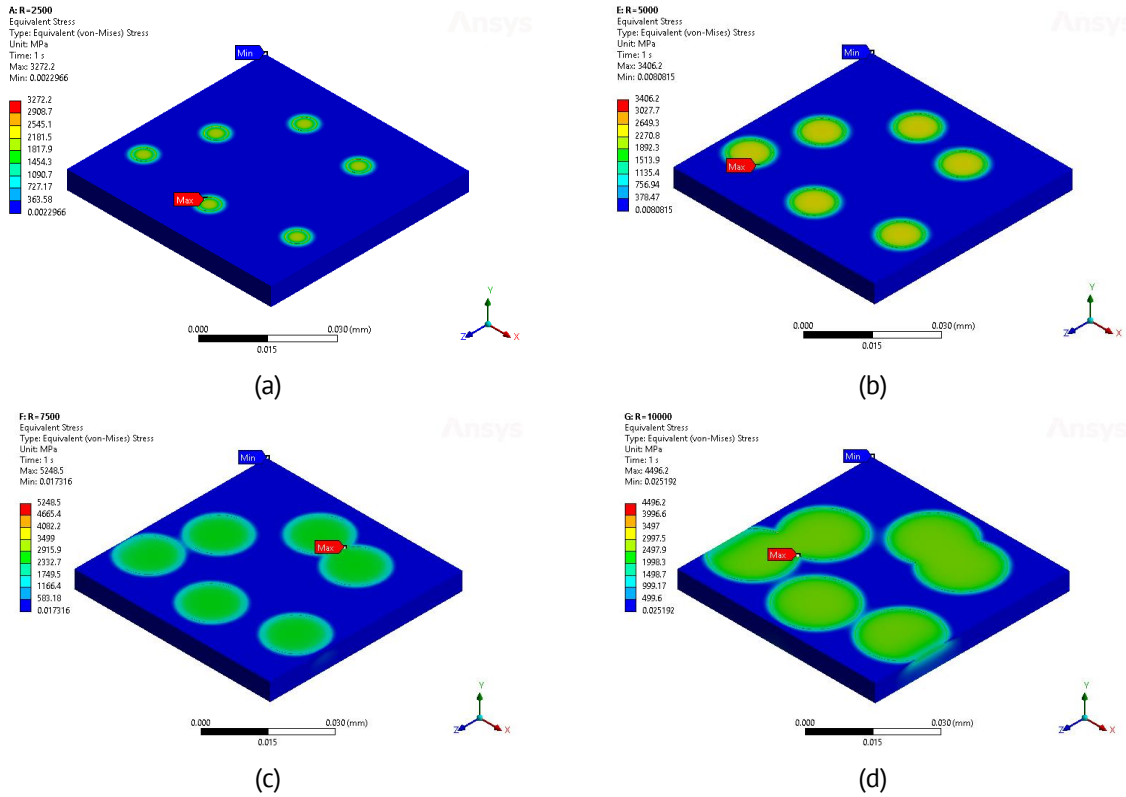

Fig. 15. Growth models of the perovskite phase in a film with a distribution of stress intensity fields according to Mises: (a) for cylindrical inclusions with a radius of 2.5 μm, (b) 5 μm, (c) 7.5 μm, and (d) 10 μm

The evolution of the von Mises stress intensity fields during the growth of six cylindrical inclusions is shown in Fig. 15. As the radius of the perovskite inclusion increases, the von Mises stress intensity increases simultaneously. This process continues until the intersection of two inclusions, where stress concentrators are formed (Fig. 15(c,d).

To determine the extent to which the distance between perovskite phase inclusions influences the configurational force, two stages of perovskite growth development were considered. At these stages, the radiuses of the cylindrical inclusion were R_1 = 2.5 μm and R_2 = 10 μm. Two paths were defined for the study the degree of influence when the distance between the inclusion centers was L_1 = 25.7 μm and L_2 = 34.4 μm. Consider points A_1, A_2, B_1 and B_2, which are defined as shown in Fig. 16. Point A_1 is located at the boundary of the perovskite and pyrochlore phases on the L_1 trajectory, when the perovskite phase develops for the R_1 cylinder radius. Point A_2 is located at the boundary of the perovskite and pyrochlore phases on the L_2 trajectory, when the perovskite phase develops within the R_1 cylinder radius. Point B_1 is located at the boundary between the perovskite and pyrochlore phases along trajectory L_1, when the perovskite phase develops within the radius of cylinder R_2. Point B_2 is located at the boundary between the perovskite and pyrochlore phases along trajectory L_2, when the perovskite phase develops within the radius of cylinder R_2.

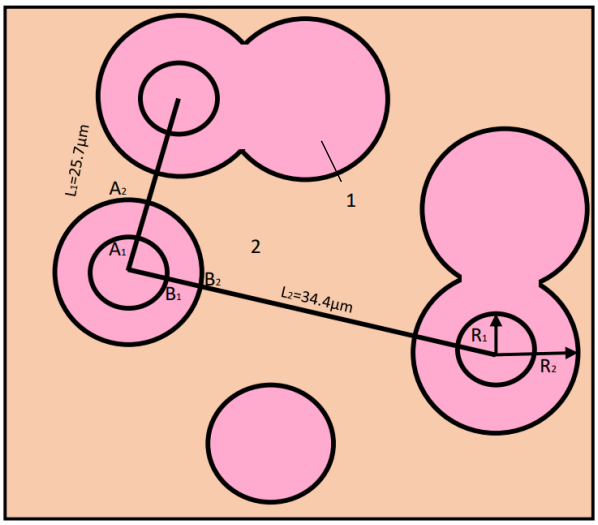

Fig. 16. Geometry parameters for representative volume element of PZT film for multiple cylindrical inclusions. 1 - perovskite inclusions, 2 - pyrochlore matrix

The study demonstrated that the configuration force is related to two geometric parameters: the first is the distance between the centers of the perovskite inclusions 2ρ, and the second is the radius of the perovskite inclusion R. The configuration force increase with decreasing perovskite inclusion radius and with decreasing distance between the centers of the perovskite inclusions.

The greatest configurational force was observed at point A_1 (Fig. 17(b)), which was located at the interphase boundary at the smaller radius and on the first path L_1. The next largest configurational force, which was 50 % lower, was at point B_1. The next largest

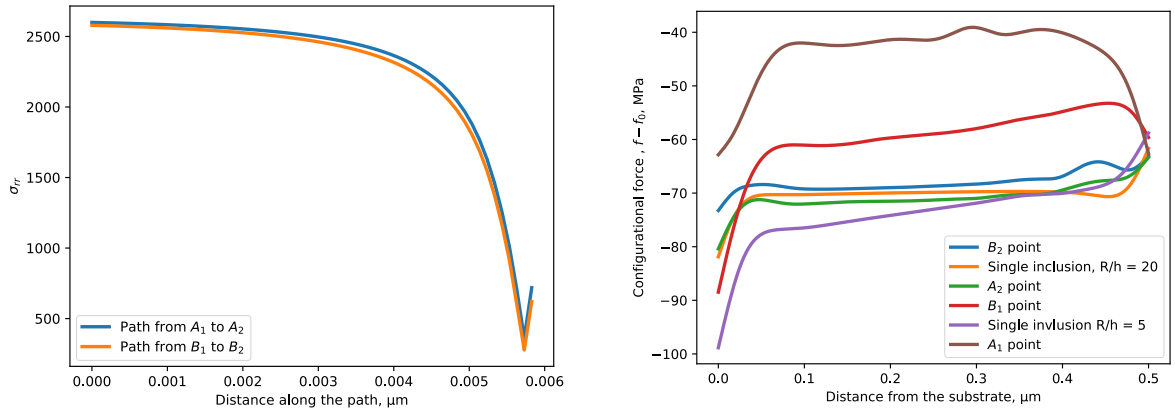

Fig. 17. Dependencies of (a) the radial stress σ_{rr} [MPa] vs the distance from the spherulite center and (b) the configurational force f_N vs the distance to the substrate (vertical coordinate z) at different ratios of the inclusion radius to the film thickness *R/h* in the 3D model of growth of 6 perovskite inclusions

configuration force, which was 16 % lower, was at point B_2. The configurational force, amounting to 7 % less, was observed at point A_2. It has been observed that configurational force in point B_2 exhibits a greater magnitude than in point A_2. This is explained by the influence of the perovskite inclusion, located at the other end of path L_1, on the configurational force.

The radial distributions of radial stresses σ_{rr} along two different orthogonal directions L_1 and L_2 differ very little (Fig. 17(a)). It is evident that as one moves away from the center of the spherulite, the radial stresses decrease.

Comparison of growth axis deviation angles for different deformation mechanisms and with experimental data

The rotation of the crystal-lattice growth axis in growing spherulitic islands, as well as in the resulting spherulitic block structure observed in experiments on PZT films [10–14], is a consequence of the significant mechanical stresses induced by changes in film density during crystallization of the perovskite phase. The growth axes exhibit axial symmetry and are oriented radially from the center of each spherulitic island toward its periphery.

The growth axis rotation rate $\frac{\partial \beta}{\partial r}$ measured in experiments using XRD analysis and scanning electron microscopy methods, lies in range of ~ 0.5÷1.4 deg/μm [10–14]. The rotation rate calculated from Eq. (7) with n = 0.32 and $z = h / 2$, is equal 0.4 deg/μm for axisymmetric elastic formulation (see section “Elastic solution”) and 0.8 deg/μm for axisymmetric elastoplastic formulation (see section “Elastoplastic solution”). These results are consistent to the order of magnitude observed in the experiments.

However, in addition to the mechanism of growth-axis rotation caused by the nonuniform distribution of configurational forces along the film thickness during the pyrochlore → perovskite phase transition, which was discussed in detail above, alternative mechanisms of film deformation are also possible. These include deviations of the perovskite growth axes due to:

1. bending of a multilayer plate (taking into account the compliance of the substrate) due to nonuniform initiated by the pyrochlore → perovskite phase transition [14];

2. bending of a multilayer plate due to polarization associated with the paraelectric → ferroelectric phase transform [33];
3. bending of a multilayer plate during cooling from 580 to 21 °C due to mismatches in coefficients of thermal expansion [34].

Growth axis rotation rate (bending plate curvature) for the first deformation mechanism was performed with assuming constant transformational deformation within the film based on Eqs. (18) from [14]:

$$\frac{\partial\beta}{\partial r} = \kappa^{tr} = \frac{\varepsilon^*}{H}\frac{6\frac{\bar{E}_{PZT}h}{\bar{E}_{Si}H}\left(1+\frac{h}{H}\right)}{1+2\frac{\bar{E}_{PZT}h}{\bar{E}_{Si}H}\left(2+3\frac{h}{H}+2\frac{h^2}{H^2}\right)+\frac{\bar{E}_{PZT}^2h^4}{\bar{E}_{Si}^2H^4}}, \quad (12)$$

where for double-layered plate $\bar{E}_i = \frac{E_i}{1-\nu_i}$, in the film i = PZT ($0 \le z \le h$), in the substate i = Si ($-H \le z \le 0$), $\varepsilon^{*Py\to Pe} = -0.0267$.

Equation (12) can also be used for calculating the rotation growth rate (plate curvature) for the second deformation mechanism, which arises from polarization associated with the paraelectric → ferroelectric phase transformation with $\varepsilon^{*Pa\to Fe} = 0.0073$ [35] ([36–38] provide data ranging from 0.0020 to 0.0191).

Equation (12) for calculating the rotation growth rate for the third deformation mechanism, which arises during cooling from 580 to 21 °C due to mismatches in coefficients of thermal expansion, has the form:

$$\frac{\partial\beta}{\partial r} = \kappa^{T} = \frac{(\alpha_{PZT}-\alpha_{Si})\Delta T}{H}\frac{6\frac{\bar{E}_{PZT}h}{\bar{E}_{Si}H}\left(1+\frac{h}{H}\right)}{1+2\frac{\bar{E}_{PZT}h}{\bar{E}_{Si}H}\left(2+3\frac{h}{H}+2\frac{h^2}{H^2}\right)+\frac{\bar{E}_{PZT}^2h^4}{\bar{E}_{Si}^2H^4}}. \quad (13)$$

In the rotation growth axis rate calculations according to Eqs. (10) and (11) the following parameter values were used E_{PZT} = 70 GPa, E_{Si} = 109 GPa, α_{PZT} = 9.0·10^{-6} 1/K, α_{Si} = 4.2·10^{-6} 1/K, h = 500 nm, H = 5 μm, $\varepsilon^{*Py\to Pe} = -0.0267$, $\varepsilon^{*Pa\to Fe} = 0.0073$, ΔT = 559 K. Calculations were performed assuming constant transformation deformation and thermal deformation in the film.

Comparison of the growth axis rotation rate caused by various deformation mechanisms is shown in Fig. 17. It can be seen that the dominant contribution arises from

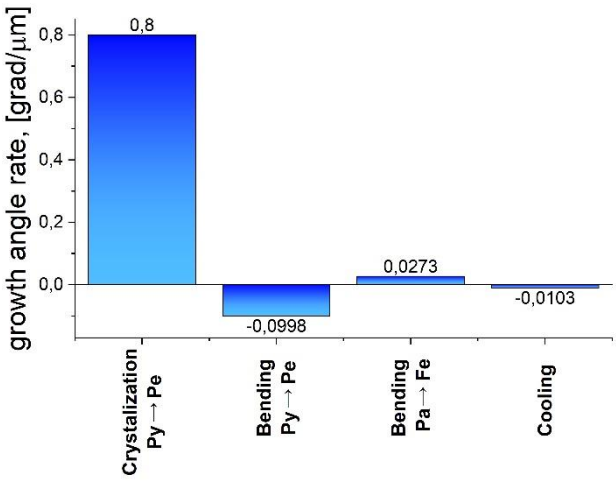

Fig. 18. Comparison of the growth axis rotation rate caused by various deformation mechanisms

nonuniform distribution of configurational forces along film thickness. The rotational rates resulting from plate bending due to nonuniform stress distribution, associated with pyrochlore → perovskite phase transition [14], bending due polarization associated with paraelectric → ferroelectric phase transition [33], bending during cooling due to mismatches in coefficients of thermal expansion are significantly smaller. Calculations were performed assuming the substate thickness equal 10 thickness of the film. As the substrate thickness increases and the film thickness decreases, the influence of the three deformation mechanisms under consideration will decrease.

Conclusion

The results of the interphase boundary propagation during the growth of the perovskite phase within a pyrochlore matrix in thin PZT films, carried out using configurational-force mechanics, are presented. The nonuniform distribution of configurational forces along the film thickness leads to a dependence of the interphase-boundary propagation velocity on the vertical coordinate. This, in turn, causes a progressive tilt and curvature of the interphase boundary away from the center of the spherulite, thereby determining the orientation of the growth axis of the emerging perovskite phase.

The growth of cylindrical, conical, and spherical inclusions was analyzed. For cylindrical inclusions, the dependence of the configurational force on distance from substate is nearly linear (monotonically increasing with distance from the substrate), which leads to a progressive deviation of both the interphase boundary and the growth axis from the vertical as the distance from the spherulite center increases. For conical inclusions with small cone angles, the configurational-force distribution along the height is monotonically increasing, whereas for large cone angles it becomes monotonically decreasing. This behavior indicates the existence of a characteristic slope toward which the growth axis asymptotically tends as the interphase boundary propagates. In spherical inclusions, more intensive growth in the vertical direction is observed near the substrate, while on the free surface growth in the radial direction dominates. At large radius, the model of a spherical inclusion reduces to a conical inclusion.

A comparison of the solutions obtained using linear elastic and elastic–plastic formulations showed that the latter yields lower values of configurational forces. The elastic–plastic formulation indirectly accounts for the presence of dislocations, micropores, and microcracks. Solving the problem within an elastic–plastic framework also demonstrated the possibility of a linear increase of the growth axis rotation angle, consistent with experimental observations.

A comparison of the numerical solutions obtained in axisymmetric and three-dimensional settings for an elementary representative volume (regular inclusions) demonstrated good agreement, with differences of less than 10 %.

The results of a comparison between the growth of single inclusions and multiple inclusions arranged regularly or irregularly are presented. The same radial distribution pattern (axial symmetry) is observed on the free surface of the film for different angles within an inclusion (a growing spherulite) surrounded by neighboring inclusions located at various distances.

The dominant influence on the growth axis rotation angle is exerted by the non-uniform distribution of the configurational force along the film thickness during the pyrochlore → perovskite phase transition. The rotation associated with plate bending caused by stress inhomogeneities initiated by the pyrochlore → perovskite phase transition, polarization during the paraelectric → ferroelectric phase transition, and due to differences in the thermal expansion coefficients of individual layers are much smaller (at least six times lower). This indicates that the distribution of configurational forces across the film thickness is the primary mechanism determining the orientation of the growth axis. The predicted rate of growth-axis deviation as a function of the distance from the spherulite center, obtained using this approach, correlates well with experimental data from X-ray diffraction analysis and scanning electron microscopy.

CRediT authorship contribution statement

Madyan Bakkar: investigation, writing – review & editing, original draft, data curation; **Alaa Mhemeed Dbes:** investigation, writing, review & editing; **Dmitrij V. Avdonyushkin:** investigation, data curation, writing; **Artem S. Semenov**: conceptualization, writing – review & editing, supervision.

Conflict of interest

The authors declare that they have no conflict of interest.

References

1. Uchino K. *Ferroelectric Devices*. New York: Decker; 2000.
2. Waser R. *Nanoelectronics and Information Technology: Advanced Electronic Materials and Novel Devices*. Berlin: Wiley-VCH; 2005.
3. Abdullaev DA, Milovanov RA, Volkov RL, Borgardt NI, Lantsev AN, Vorotilov KA, Sigov AS.Ferroelectric memory: state-of-the-art manufacturing and research. *Russian Technological Journal*. 2020;8(5): 44–67. (In Russian)
4. Ishiwara H, Arimoto Y, Okuyama M. *Ferroelectric Random Access Memories: Fundamentals and Applications*. Berlin: Springer; 2004.
5. Izyumskaya N, Alivov YI, Cho SJ, Morkoç H, Lee H, Kang YS. Processing, structure, properties, and applications of PZT thin films. *Critical Reviews in Solid State and Materials Sciences*. 2007;32(3–4): 111–202.
6. Eom CB, Trolier-McKinstry S. Thin-film piezoelectric MEMS. *MRS Bulletin*. 2012;37(11): 1007–1021.
7. Panda PK, Sahoo B. PZT to Lead Free Piezo Ceramics: A Review. *Ferroelectrics*. 2015;474(1):128–143.
8. Mukhortov VM, Yuz'uk YI. *Heterostructures Based on Nanosized Ferroelectric Films: Preparation, Properties and Applications*. Rostov-on-Don: Southern Scientific Center of the Russian Academy of Sciences; 2008. (In Russian)
9. Gevorgian S. *Ferroelectrics in Microwave Devices, Circuits and Systems*. London: Springer; 2009.
10. Staritsyn MV, Pronin VP, Khinich II, Senkevich SV, Kaptelov EY, Pronin IP, Elshin AS, Mishina ED. Microstructure of spherulitic lead zirconate titanate thin films. *Physics of the Solid State*. 2023;65(8): 1312–1318.
11. Kiselev DA, Staritsyn MV, Senkevich SV, Kaptelov EY, Pronin IP, Pronin VP. Radially oriented lateral self-polarization in spherulitic islands of lead zirconate titanate thin films. *Technical Physics Letters*. 2023;49(22): 8–11. (In Russian)
12. Kukushkin SA, Tentyilova IY, Pronin IP. Mechanism of the phase transformation of the pyrochlore phase into the perovskite phase in lead zirconate titanate films on silicon substrates. *Phys. Solid State*. 2012;54: 611–616.
13. Pronin VP, Ryzhov IV, Staritsyn MV, Senkevich SV, Kaptelov EY, Pronin IP. An influence of mechanical stresses on the phase state of spherulitic thin films of lead zirconate titanate. *Materials Physics and Mechanics*. 2024;52(6): 17–26.
14. Avdonyushkin DV, Staritsyn MV, Pronin VP, Semenov AS, Senkevich SV, Pronin IP. The Influence of Mechanical Stresses on Formation of Thin Spherulite PZT Films. To be published in *Physical Mesomechanics*. [Preprint] 2026.

15. Senkevich SV. *Features of Crystallization and Ferroelectric Properties of Thin Polycrystalline Lead Zirconate Titanate Films Obtained by a Two-Stage Method [dissertation].* Saint Petersburg; 2011. (In Russian)
16. Gushchina EV, Osipov VV, Borodin BR, Pavlov S, Tolmachev VA, Dunaevskiy MS, et al. Piezoelectric, conductive, and dielectric properties of magnetron sputtered $PbZr_{54}Ti_{46}O_3$ films studied by scanning probe microscopy and spectroscopic ellipsometry methods. *Ferroelectrics.* 2019;541(1):47–53.
17. Dolgintsev DM, Kaptelov EY, Senkevich SV, Pronin IP, Pronin VP. Microstructure and properties of polycrystalline PZT films obtained by RF magnetron sputtering with fine variation of the composition near morphotropic phase boundary. *Physics of Complex Systems.* 2021;2(3):101–109.
18. Lobanov SM, Semenov AS, Mamchits A. Modeling of Hysteresis in Single-Crystalline Barium Titanate with Allowance for Domain Structure Evolution. *Phys Mesomech.* 2023;26: 167–175.
19. Eshelby JD. The force on an elastic singularity. *Phil Trans Roy Soc London A.* 1951;244: 87–112.
20. Gurtin ME. On the nature of configurational forces. *Arch Ration Mech Anal.* 1995;131: 67–100.
21. Gurtin ME. *Configurational Forces as Basic Concepts of Continuum Physics.* New York: Springer; 2000.
22. Kienzler R, Herrmann G. *Mechanics in Material Space.* Berlin: Springer; 2000.
23. Maugin GA. *Material Inhomogeneities in Elasticity.* London: Chapman & Hall; 1993.
24. Maugin GA. Material forces: concepts and applications. *Appl Mech Rev.* 1995;48(5): 213–245.
25. Steinmann P, Scherer M, Denzer R. Secret and joy of configurational mechanics: From foundations in continuum mechanics to applications in computational mechanics. *Z Angew Math Mech.* 2009;89(8): 614–630.
26. Freidin AB. On configurational forces in the mechanics of phase and chemical transformations. *Journal of Applied Mathematics and Mechanics.* 2022;86(4): 571–583.
27. Freidin AB. On new phase inclusions in elastic solids. *ZAMM - Journal of Applied Mathematics and Mechanics.* 2007;87(2): 102–116.
28. Freidin AB, Vilchevskaya EN, Korolev IK. Stress-assist chemical reactions front propagation in deformable solids. *International Journal of Engineering Science.* 2014;83: 57–75.
29. Kabanova PK, Freidin AB. On the localization of a new phase domain in the vicinity of an elliptical hole. *ZAMM - Journal of Applied Mathematics and Mechanics.* 2024;104(3): e202301035.
30. Kabanova P, Morozov A, Freidin AB, Chudnovsky A. Numerical simulations of interface propagation in elastic solids with stress concentrators. In: Altenbach H, Bruno G, Eremeyev VA, Gutkin MYu, Müller WH. (eds.) *Mechanics of Heterogeneous Materials.* Springer; 2023. p.201–217.
31. Kabanova PK, Freidin AB. Numerical investigation of the evolution of new phase domains in an elastic solid. *Comput. Contin. Mech.* 2022;15(4): 466–479. (In Russian)
32. Helean KB, Ushakov SV, Brown CE, Navrotsky A, Lian J, Ewing RC, et al. Formation enthalpies of rare earth titanate pyrochlores. *Journal of Solid State Chemistry.* 2004;177(6): 1858–1866.
33. Korchagin AP, Semenov AS. Finite-element modeling of the polarization process of a ferroelectric multilayer structure due to the of microstresses during cooling. In: *Proceedings of the All-Russian Scientific Conference "Science Week PhizMech".* Saint Petersburg; 2023. p.273–276. (In Russian)
34. Valeeva AR, Kaptelov EY, Pronin IP, Senkevich SV, Pronin VP. Mechanical stresses in lead zirconate titanate thin films formed on substrates differing in temperature coefficients of linear expansion. *Physics of Complex Systems.* 2022;3(4): 159–166.
35. Semenov AS. *Multilevel Models of Ferroelectroelastic Materials and Their Application for Solution of Boundary Value Problems [dissertation].* Saint Petersburg; 2022. (In Russian)
36. Jaffe B, Cook WR, Jaffe H. *Piezoelectric Ceramics.* New York: Academic Press; 1971.
37. Semenov AS. Micromechanical Model of a Polycrystalline Ferroelectrelastic Material with Consideration of Defects. *J Appl Mech Tech Phys.* 2019;60: 1125–1140.
38. Semenov AS. A microstructural model of ferroelectroelastic material with taking into account the defects' evolution. *St. Petersburg Polytechnical State University Journal. Physics and Mathematics.* 2021;14(1): 31–54.